A&A, 688, A4 (2024)
https://doi.org/10.1051/0004-6361/202449343

Astronomy & Astrophysics

Minimalist model of the W50/SS433 extended X-ray jet: Anisotropic wind with recollimation shocks

E. M. Churazov[1,2], I. I. Khabibullin[3,2,1], and A. M. Bykov[4]

[1] Max Planck Institute for Astrophysics, Karl-Schwarzschild-Str. 1, 85741 Garching, Germany
e-mail: churazov@mpa-garching.mpg.de
[2] Space Research Institute (IKI), Profsoyuznaya 84/32, Moscow 117997, Russia
[3] Universitäts-Sternwarte, Fakultät für Physik, Ludwig-Maximilians-Universität München, Scheinerstr.1, 81679 München, Germany
[4] Ioffe Institute, Politekhnicheskaya st. 26, Saint Petersburg 194021, Russia

Received 25 January 2024 / Accepted 15 April 2024

ABSTRACT

W50 is a radio nebula around the hyperaccreting Galactic microquasar SS433. We focus on one peculiar feature of W50, that is, on a pair of so-called extended X-ray jets (EXJs). These jets have a size of ∼20 pc and a sharp inner boundary, and their spectra are well represented by a featureless X-ray continuum. We argue that EXJs could be an outcome of a powerful anisotropic wind produced by a supercritical accretion disk. In the simplest version of this model, the wind itself consists of two components. The first component is a nearly isotropic outflow that subtends most of the solid angle as seen from the compact source and creates the quasi-spherical part of the W50 nebula. The second component is a more collimated wind that is aligned with the rotation axis of the binary system (polar wind). The isotropic outflow passes through the termination shock, and its increased thermal pressure creates a sequence of recollimation shocks in the polar wind, giving it the appearance of an extended X-ray structure. In this model, the EXJ continuum spectrum is due to synchrotron emission of electrons that are accelerated at the shocks that arise in the polar wind. At variance with many other studies, the EXJ structures in this model are not directly related to the highly collimated and precessing 0.26 c baryonic jets. Instead, the EXJ and the ears of W50 are produced by the part of the wind whose Eddington-level kinetic luminosity is confined to a half-opening angle of 5–10 degrees. This is not necessarily a recollimated version of the 0.26 c jets.

Key words. acceleration of particles – plasmas – shock waves – cosmic rays – ISM: jets and outflows

1. Introduction

W50 and SS433 represent a prototypical combination of a giant radio-bright nebula and a hyperaccreting compact source that powers the nebula (see, e.g., Margon 1984; Fabrika 2004 for reviews). Many properties of W50/SS433 remain poorly understood, partly because rare and short-living hyperaccreting black holes or neutron stars might operate in a very different regime than the more ubiquitous and better-studied sub-Eddington sources (e.g., Fabrika et al. 2015). In this regard, the stability of the properties of SS433 over more than 40 years of observations (e.g., Cherepashchuk et al. 2021) makes it a particularly appealing laboratory for an exploration of hyperaccretors (e.g., Begelman et al. 2006).

It has been shown that the binary system in SS433 can avoid forming a common envelope and sustain an extremely high accretion rate (about a few hundred times the Eddington level) for a long time, $t_{\rm life} \sim 10^4$–10^5 yr (van den Heuvel et al. 2017; Cherepashchuk et al. 2023). A simple estimate of the total energy that might be injected by such a source into the surrounding medium is $E_{\rm inj} \sim L_{\rm Edd} t_{\rm life} \sim 3 \times 10^{50} L_{39} t_4$ erg, where $L_{39} = L_{\rm Edd}/10^{39}$ erg s^{-1} and $t_4 = t_{\rm life}/10^4$ yr. This is comparable to the energy output of a supernova explosion that has created the compact object of the binary in the first place. As a result, such an object can strongly affect the interstellar medium (ISM) in the vicinity of the binary, creating and powering a giant $\gtrsim$10 pc nebula (e.g., Begelman et al. 1980).

A key prediction of the standard accretion theory in the highly supercritical regime (Shakura & Sunyaev 1973) is that a large fraction of liberated gravitational energy of the accreted material is channeled into powerful trans- and mildly relativistic outflows with various degrees of axial collimation (see Yoshioka et al. 2022, for recent numerical simulations). One of the most notable features of SS433, the transrelativistic baryonic jets with their bulk velocity $v \sim 0.26\,c$ and an opening angle smaller than 2 degrees, appears to be a direct confirmation of this prediction (e.g., Begelman et al. 1980; Calvani & Nobili 1981). These narrow jets reveal themselves in X-ray and optical spectra as pairs of blue- and redshifted lines, coming from the vicinity ($\lesssim 10^{12}$ cm and $\lesssim 10^{15}$ cm for the X-ray and optical lines, respectively) of the compact source (Fabrika 2004; Blundell et al. 2018; Waisberg et al. 2019). Modeling of these lines demonstrated that the kinetic luminosity of the jets is indeed comparable to the Eddington luminosity of a stellar mass black hole (Marshall et al. 2002, 2013; Brinkmann et al. 2005; Medvedev & Fabrika 2010; Khabibullin et al. 2016; Medvedev et al. 2019; Fogantini et al. 2023). The baryonic jets, however, remain invisible beyond a distance of ∼0.1 pc from the central source, where they manifest themselves as a spectacular time-variable corkscrew pattern of the radio emission due to the precession of the narrow jet direction with a period of 163 days and a half-amplitude of 20 degrees (e.g., Hjellming & Johnston 1981; Blundell & Bowler 2004)[1].

[1] The nature of the diffuse X-ray emission detected by the *Chandra* Observatory from a similar location (so-called "arcsec-scale X-ray emission", Migliari et al. 2002) is less clear (e.g., Khabibullin & Sazonov 2017), given its irregular variability and peculiar spectral features (Migliari et al. 2005; Miller-Jones et al. 2008).

Since at even larger scales from 40 to 110 pc, SS433 is surrounded by the radio- and Hα-bright nebula W50, which is strongly elongated (with an aspect ratio of 3:1) along the precession axis of the jets, it has long been considered that the kinetic energy of these strongly collimated jets powers and shapes the W50 nebula (Begelman et al. 1980; Zealey et al. 1980; Eichler 1983; Peter & Eichler 1993; Velázquez & Raga 2000; Zavala et al. 2008; Goodall et al. 2011; Asahina et al. 2014; Monceau-Baroux et al. 2015; Panferov 2017; Ohmura et al. 2021).

The question remains open whether the narrow jets power the entire nebula. The radio, optical, and X-ray images of W50 indeed lack direct observational signatures of recollimation or termination of the narrow jets (like termination hot spots or a clear pattern of the decelerating flow, see, e.g., Dubner et al. 1998; Goodall et al. 2011; Farnes et al. 2017; Broderick et al. 2018). Instead, very peculiar elongated X-ray structures are seen on both sides of SS433 (e.g., Watson et al. 1983; Yamauchi et al. 1994; Safi-Harb & Ögelman 1997; Safi-Harb & Petre 1999; Brinkmann et al. 2007; Safi-Harb et al. 2022). These features, which we call extended X-ray jets (EXJs), are separated from the binary by ∼20 pc, are aligned with the narrow jet precession axis, and have an opening angle of ∼20° (i.e., twice smaller than the precession amplitude of the compact jets). They are characterized by a hard featureless X-ray spectrum that gradually steepens with distance from SS433 (e.g., Brinkmann et al. 2007; Safi-Harb et al. 2022).

The synchrotron origin of these structures is not only attractive from the points of view of spectral and energy and mass requirements (e.g., Brinkmann et al. 2007), but also leads to verifiable predictions regarding the very high energy (VHE) gamma-ray emission coming from them (Safi-Harb & Ögelman 1997; Aharonian & Atoyan 1998; Reynoso et al. 2008; Kimura et al. 2020; Sudoh et al. 2020). The advent of modern VHE observatories allowed the detection of extended emission from W50 (cospatial with EXJ) at TeV energies (Abeysekara et al. 2018). Another important implication of the synchrotron scenario is the possibility of a high degree of polarization, provided that the magnetic field is globally ordered inside these lobes. The recent observation of the eastern lobe by the Imaging X-ray Polarimetry Explorer (IXPE) revealed a high degree of X-ray polarization and suggest that the magnetic field is aligned with the main axis of the system (Kaaret et al. 2024).

In this paper, we propose a model that attempts to associate the overall W50 morphology and EXJs with an anisotropic wind from the binary system. In this model, an almost isotropic part of the wind causes the quasi-spherical part of the W50 nebula, while a more collimated portion of the wind drives the ears of W50. In the same framework, the termination of the isotropic wind sends recollimation shocks into the collimated wind, giving rise to the EXJ features.

2. Basic model

We want to explain the following salient characteristics of the EXJs associated with W50:

- The sharp inner boundary of the EXJ in X-rays on both sides from SS433 and the lack of bright emission in optical and radio bands.
- The featureless EXJ X-ray spectrum, which can (empirically) be described as either thermal bremsstrahlung with $kT \sim 4$ keV or as a power law with a photon index $\Gamma \sim 2.2$ (Brinkmann et al. 2007). From the joint analysis of *XMM-Newton* and *NuSTAR* data, Safi-Harb et al. (2022) derived a flatter spectrum $\Gamma \sim 1.6$ for the EXJ portion closest to the SS433 and $\Gamma \sim 2.05$ for the lenticular region that is further away (based on the data of *XMM-Newton* alone).

The usual assumption is that an outer boundary of the W50 nebula model is a forward shock associated with the supernova explosion and a jet or outflow (e.g., Goodall et al. 2011). Since the inner boundary of EXJ is closer to the binary than the quasi-spherical part of W50, it is difficult to associate it with any characteristic radius. We instead assumed that the entire nebular is powered by a wind produced by SS433. The wind has an additional characteristic radius, that is, a termination shock, which we associate with the inner boundary of EXJ. A wind from a companion star was considered by Konigl (1983), while Asahina et al. (2014) assumed that the wind is produced by the super-Eddington accretion onto the compact object, which is similar to the assumption adopted here. For the mechanical wind power of $\sim 10^{39}$ erg s^{-1}, the total energy produced by the wind over the estimated age of $\sim 6 \times 10^4$ yr is $\sim 2 \times 10^{51}$ erg, which is on the same order or even higher than the kinetic energy of a supernova (SN) ejecta. We ignored the contribution of the SN energy input, although this scenario is often assumed. For our model, the most important is that at the present epoch, the powerful wind is present and has already been operating for a sufficiently long time. We briefly discuss this case in Appendix B.

A steady isotropic wind model (Chevalier & Clegg 1985) is characterized by a set of four parameters (assuming that the wind is supersonic): L_w, v_w, t_age, and n_0, which are the wind kinetic power, the wind velocity, the age of the system, and the density of the interstellar medium (ISM), respectively. The latter is assumed to be homogeneous and uniform. In the frame of this model, these four parameters can be estimated from several basic observables, such as the radius of the nebula and the gas temperature downstream of the shock driven by the wind.

A typical radial structure of the wind expanding into a uniform medium is shown in Fig. 1. It consists of a forward shock advancing into the ISM, a wind termination shock, and a contact discontinuity, separating the shocked ISM from the shocked wind material. We associate the quasi-spherical part of the W50 nebula with the forward shock. When we assume that the forward shock is strong and adopting the downstream temperature of the gas of $T_\mathrm{s} \sim 0.2$ keV (e.g., Brinkmann et al. 2007; Safi-Harb et al. 2022), the shock velocity is

$$v_\mathrm{s} = \left(\frac{16}{3}\frac{kT_\mathrm{s}}{\mu m_\mathrm{p}}\right)^{1/2} \approx 410\left(\frac{kT_\mathrm{s}}{0.2\ \mathrm{keV}}\right)^{1/2}\ \mathrm{km\ s^{-1}}. \quad (1)$$

The estimate of the age of the system for a supersonic expansion, that is, $R_\mathrm{s} \propto t^{3/5}$ is then

$$t_\mathrm{age} \approx \frac{3}{5}\frac{R_\mathrm{s}}{v_\mathrm{s}} = 5 \times 10^4 \left(\frac{R_\mathrm{s}}{38\ \mathrm{pc}}\right)\left(\frac{v_\mathrm{s}}{410\ \mathrm{km\ s^{-1}}}\right)^{-1}\ \mathrm{yr}, \quad (2)$$

while the power of the wind is

$$L_\mathrm{w} \approx \frac{\frac{4}{3}\pi R_\mathrm{s}^3 \frac{9}{4} n_0 \mu m_\mathrm{p} v_\mathrm{s}^2}{t_\mathrm{age}} =$$

$$7 \times 10^{38}\left(\frac{n_0}{0.1\ \mathrm{cm^{-3}}}\right)\left(\frac{R_\mathrm{s}}{38\ \mathrm{pc}}\right)^2\left(\frac{kT_\mathrm{s}}{0.2\ \mathrm{keV}}\right)^{3/2}\ \mathrm{erg\ s^{-1}}, \quad (3)$$

where n_0 is the particle number density of the unshocked ISM, $\mu \approx 0.61$ is the mean atomic weight per particle for the fully ionized gas with a standard cosmic composition. We assumed that the forward shock is strong and the energy density is constant across the entire volume subtended by the shock. Of the

three observables used above, namely R_s, T_s, and n_0, only R_s can easily be measured directly from X-ray or radio images, while T_s and n_0 can only be robustly determined from X-ray spectra when the shock-heated ISM has reached collisional ionization equilibrium (and $T_e \approx T_i$), which is not guaranteed a priori. We therefore used some fiducial values for T_s and n_0, but acknowledge that their values (except for R_s) are uncertain by a factor of a few. For instance, the density n_0 can be lower and the post temperature T_s can be higher (see, e.g., the nonequilibrium ionization model in Brinkmann et al. 2007), making the estimate power uncertain in either direction. In particular, their best-fitting estimate of the ionization time $n_e t \sim 3 \times 10^{10}\,\mathrm{s\,cm^{-3}}$ for $n_0 \sim 0.1\,\mathrm{cm^{-3}}$ (for ionized plasma with a solar abundance of the elements, $n_e \approx 0.52\,n_0$) translates into $t \sim 2 \times 10^4$ yr. It is therefore plausible that the actual density of the ambient medium is lower by a factor of a few.

The velocity of the wind v_w could be estimated if the radius of the wind termination shock R_T were known. The pressure is approximately constant between the forward-shock position R_s and R_T. The latter is determined from the balance of the ram pressure of the wind P_w and the postshock pressure P_s, that is,

$$P_w = \rho_w v_w^2 = \frac{L_w}{4\pi R_T^2 v_w} \sim P_s = 4\,n_0 \frac{3}{16} \mu m_p v_s^2, \quad (4)$$

where $\rho_w(R) \propto R^{-2}$ and v_w are the wind density and velocity, respectively, and the factor of 4 stands for the compression ratio at the forward shock, which is assumed to be strong. The above relation (dropping factors on the order of unity) implies that the radii of the forward and termination shocks are related via the ratio of the shock and wind velocities as

$$R_T \approx R_s \left(\frac{v_s}{v_w}\right)^{1/2}. \quad (5)$$

The isotropic wind expanding into a homogeneous medium naturally produces a spherically symmetric forward shock, a contact discontinuity, and a termination shock (see Fig. 1). The density of the shocked wind might be low enough for its thermal X-ray emission to be observed directly. Figure 1 corresponds to the Chevalier & Clegg (1985) steady wind solution. It follows from the figure that for the adopted parameters, the density downstream of the termination shock is smaller by a factor of ≈40 than that at the forward shock. Because the X-ray emissivity scales as the square of the gas density, the expected surface brightness of the termination shock region at energies below a few keV is a factor of about 10^3 smaller than for the forward shock. Moreover, the termination shock of the isotropic wind is not necessarily an efficient particle accelerator (e.g., Parizot et al. 2004). In this model, it is therefore expected that this shock creates neither radio nor X-ray emission.

The W50 nebula, however, is elongated in the direction perpendicular to the orbital plane. This suggests that the wind is anisotropic, and in particular, that it is more powerful (per unit solid angle) in this direction. To explain this morphology, a combination of an expanding spherical SN shock and a jet or outflow is often used (e.g., Goodall et al. 2011). We modeled this configuration as a two-component wind. One component was a nearly isotropic wind considered above (hereafter, i-wind), and the second component was a collimated polar wind (hereafter, p-wind) along the orbital momentum of the binary. The main difference from the other models is a termination shock of the isotropic wind that recollimates the p-wind. We reiterate here that the postulated p-wind is not the highly collimated subrelativistic jet, but a part of the wind associated with the inner regions of the accretion flow that subtends a much larger solid angle than the narrow jets.

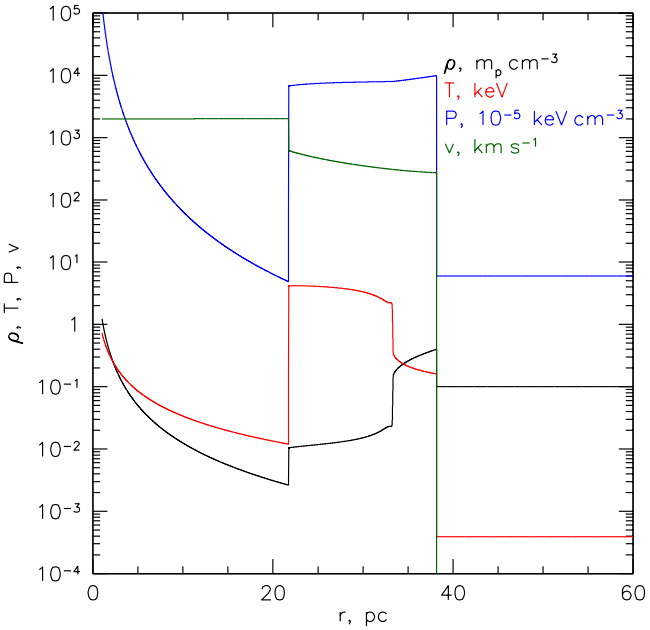

Fig. 1. Example of a spherically symmetric wind model for $\rho_{ISM} = 0.1\,m_p\,\mathrm{cm^{-3}}$, $L_w \sim 10^{39}\,\mathrm{erg\,s^{-1}}$, and $v_w = 2 \times 10^3\,\mathrm{km\,s^{-1}}$ after $t_{age} \sim 6 \times 10^4$ yr. With these parameters, the densest region is the shell of the shock-compressed ISM on the downstream side of the forward shock, which should dominate the X-ray emission of the nebula. The density of the shocked wind material is too low to produce detectable X-ray emission.

The jet propagation in astrophysical conditions has been extensively studied both theoretically and numerically (e.g., Komissarov & Falle 1998; Krause et al. 2012; Perucho & López-Miralles 2023). For example, for radio sources associated with active galactic nuclei (AGN), the canonical model identifies several characteristic length scales that determine jet propagation. These include a scale at which the jet becomes underdense with respect to the ambient gas, a scale at which the ambient pressure can counterbalance the side expansion of a conical jet, and a scale at which the ram pressure of the jet is equal to the ambient pressure. These scales determine whether the jet forms a cocoon or is recollimated by external pressure, and they determine the position of the terminal shock. In the model discussed here, the terminal shock of the isotropic wind introduces yet another length scale that modifies the behavior of the p-wind, which can itself be treated as a jet. In addition, the propagation of the p-wind occurs in the expanding i-wind, that is, the densities and pressures of the two flows have similar dependences on the radius (before reaching the i-wind termination shock). Therefore, the relation between densities and pressures was set at the base of the two flows and was further modified at the terminal shock of the i-wind (see Appendix A).

The interaction of a jet with the wind has also been studied in the context of massive binary systems (Barkov & Bosch-Ramon 2022; López-Miralles et al. 2022). There, a jet produced by an accreting black hole collides with the wind from a massive star. In the configuration considered here, we assumed that accretion on SS433 proceeds via Roche-lobe overflow (RLOF; van den Heuvel et al. 2017; Cherepashchuk et al. 2021) rather than via stellar wind. In this case, the i- and p-winds both come

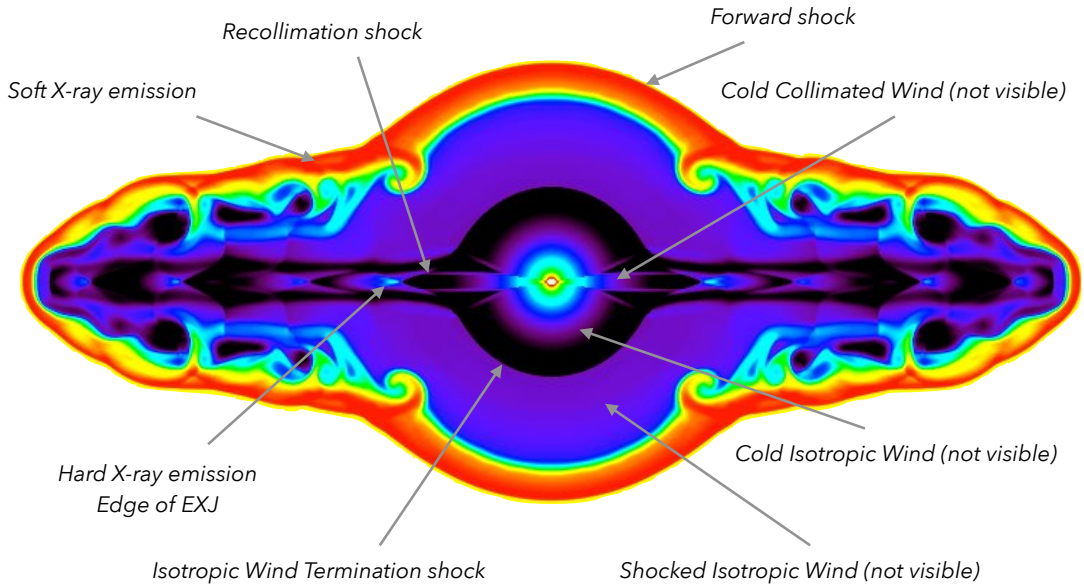

Fig. 2. Sketch of the W50 model as a combination of isotropic and polar winds. The central region represents a combination of an isotropic wind and a more collimated polar wind aligned with the orbital axis of the binary system. The isotropic wind passes through its termination shock, and the increased pressure and density recollimate the polar wind. The resulting recollimation shocks accelerate particles and give rise to the synchrotron emission of the EXJs.

from the accretion disk and move (radially) in the same direction rather than collide.

Throughout the paper, we assume that the termination radius for the p-wind is larger than for the nearly isotropic component (i.e., the dynamic pressure ρv^2 at a given radius is larger for the p-wind). This means that the material in the collimated component experiences a sudden increase in the ambient pressure when the termination shock of the i-wind is crossed. In aerodynamics, this corresponds to the case of an overexpanded jet, when the internal jet pressure at the edge of the nozzle is lower than the ambient pressure. This high pressure sends a recollimation shock into the p-wind that compresses and heats it. Therefore, an additional characteristic radius appears in the problem, which we associate with the inner boundary of EXJs well inside the forward shock. This is the essence of the model we propose.

To illustrate some basic features of the model, we ran a set of 2D simulations (axisymmetric cylindrical symmetry) using the code PLUTO (Mignone et al. 2007). The details of the simulations and the choice of parameters are described in Appendix A. A labeled sketch (density slice) is shown in Fig. 2 for $t_{\rm age} \sim 6 \times 10^4$ yr and an i-wind kinetic luminosity of 10^{39} erg s^{-1}. In supercritical accretion disks, a massive outflow starts at the spherization radius $R_{\rm sp} \approx 10\,\dot{m}_0 \frac{GM}{c^2}$ (Shakura & Sunyaev 1973; Poutanen et al. 2007), where M is the mass of the compact object, and $\dot{m}_0$ is the accretion rate in Eddington units. The corresponding escape velocity near $R_{\rm sp}$ is $v_{\rm esc} \sim \sqrt{\frac{GM}{R_{\rm sp}}} \sim c/\sqrt{10\,\dot{m}_0} \sim 3000\,{\rm km\,s^{-1}}$ for $\dot{m}_0 = 10^3$. In Fig. 2 we set $v_{\rm i} = 2000\,{\rm km\,s^{-1}}$, and in the Appendix A, we consider cases with $v_{\rm i} = 2000$ and $4000\,{\rm km\,s^{-1}}$.

The outflow continues at smaller radii of the supercritical disk. In our simplified model, we attribute these inner outflows to the p-wind component. In Fig. 2, the p-wind component is initially confined to a cone with a half-opening angle of ∼9 degrees, and its density and velocity are both higher by a factor of 2–3 than that in the i-wind. The kinetic luminosity of the p-wind is ∼14% of the i-wind. We are interested in the global picture of the nebula out to 100 pc, rather than in the vicinity of SS433. Therefore, the winds were initiated within a sphere with a relatively large radius of 8 pc. The radius of the p-wind cross section at this sphere is ∼1.3 pc. We note here that the model is flexible enough to broadly reproduce the overall morphology of the nebula for different sets of parameters, for instance, a faster p-wind or a much denser and slower p-wind (see Appendix A). However, these models share several common features that we highlight in Fig. 2. In this figure, the termination shock of the isotropic wind corresponds to the transition from the lowest density region (isotropic wind component just before the shock) to the four times higher density (downstream of the termination shock). The collimated outflow experiences a series of recollimation shocks, where the dense regions are interleaved with the lower-density patches. While the first dense region R_d does not occur exactly at the position of the isotropic wind termination shock, they are related, so that $R_d \sim O(1) \times R_T$, where the pre-factor sensitively depends on the p-wind opening angle and on the relative densities and velocities of the winds. The choice of the parameters for this simulation is rather arbitrary, and other combinations can lead to a similar morphology when the density or velocity ratios between the i-wind and p-wind are changed together with the characteristic opening angle of the p-wind. However, the recollimation shocks are always present when the i-wind termination shock is located at a radius smaller than that of the p-wind.

The above model completely neglects the contribution of the supernova explosion to W50. The primary motivation for this assumption is a mismatch between the timescale of stellar evolution (millions of years) and the duration of the period of extremely high accretion of the binary during the RLOF phase (∼10^5 yr; see, e.g., van den Heuvel et al. 2017; Cherepashchuk et al. 2023). If the former determines the onset of the RLOF after the supernova explosion, it is plausible that at the present time, the traces of the supernova remnant (SNR) are largely gone. Given the peculiar nature of SS433/W50, this

binary system might have a similarly peculiar history and the supernova explosion might have taken place some $\sim 10^5$ yr ago (e.g., Goodall et al. 2011; Panferov 2017; Bowler & Keppens 2018). We consider this possibility in Appendix B. In brief, adding $\sim 10^{51}$ erg in the form of the SN ejecta can certainly contribute to the size and shape of the nebula, but if the wind is established a sufficiently long time ago, the position of the wind termination shock is the same as shown in Fig. B.1 and the overall morphology may remain similar to the one depicted in Fig. 2.

3. Discussion

Several models have been proposed to explain the spectrum of the EXJs (e.g., Safi-Harb et al. 2022, and references therein), which they attributed to synchrotron emission. However, the origin of the EXJs themselves, which appear in the middle of nowhere, is difficult to explain.

Previously, we considered an exotic scenario for the formation of EXJ, when a very fast (subrelativistic) outflow recombines and impacts the ISM in the form of a beam of neutral atoms (Churazov et al. 2020). In this model, neutral particles penetrate the ISM, become ionized, and deposit their energy in a long and narrow channel along the direction of the beam. The heated ISM expands sideways, reducing the gas density and letting neutral particles propagate further without being ionized. This (i) leads to a fast propagation of the heating front and (ii) gives rise to a system of diverging and converging shocks perpendicular to the beam. This analysis was not specifically tied to W50/SS433, except for the assumption that neutral particles move with a velocity $\sim 0.25\,c$. In the neutral beam model, the EXJ structure forms where the beam enters the dense medium. Therefore, to explain the inner boundary of the EXJ, dense gas is required at this location.

The model we discussed in the previous section is different. It does not rely on the SS433 transrelativistic baryonic jets. Instead, it associates EXJ with the recollimation shocks in the anisotropic wind from the SS433 binary system. In this model, the isotropic part of the wind reaches the termination shock earlier than the polar wind. This translates into a condition that the momentum flux per unit solid angle is larger for the p-wind,

$$\rho_\mathrm{p} v_\mathrm{p}^2 > \rho_\mathrm{i} v_\mathrm{i}^2, \tag{6}$$

which is equivalent to the condition

$$\frac{L_\mathrm{p}}{\Omega_\mathrm{p} v_\mathrm{p}} > \frac{L_\mathrm{i}}{\Omega_\mathrm{i} v_\mathrm{i}}, \tag{7}$$

where L_p and L_i are the kinetic luminosities of the p- and i-winds, respectively, and Ω_p and Ω_i are the corresponding solid angles subtended by the winds. In the illustrative example shown in Fig. 2, $\rho_\mathrm{p} v_\mathrm{p}^2 \approx 13 \rho_\mathrm{i} v_\mathrm{i}^2$, the above condition is satisfied.

Downstream of the termination shock in the isotropic wind, the gas becomes hot and four times denser. As mentioned above, the gas density is too low to give rise to observable thermal (bremsstrahlung) emission. The termination shock of the i-wind resembles the case of an almost perpendicular shock (the upstream magnetic field is along the shock front) similar to stellar winds around massive stars. No signature of synchrotron X-ray emission was ever reported from the termination shocks of fast radiation-driven winds of young massive stars. The particle acceleration there is likely much less efficient than that in supernova shocks of similar velocity (e.g., Drury et al. 2001; Parizot et al. 2004). The cosmic-ray acceleration in the vicinity of the solar wind termination shock (with a speed higher than 400 km s^{-1}) directly measured by the Voyager missions is also rather modest (Rankin et al. 2022). The recent modeling of CR acceleration by stellar wind bubbles of young massive stars by Meyer (2024) demonstrated that the systems can mostly reaccelerate preexisting cosmic ray particles at the bubble forward shocks and do not accelerate CRs at the wind termination shocks. Thus, the particle acceleration of the i-wind termination shock is not highly efficient. In contrast, the system of recollimation shocks that formed due to i- and p-wind collisions can have a much more complicated structure of the magnetic fields, involving both a quasi-parallel and a quasi-perpendicular region. We simply assumed that the acceleration of particles in the recollimated p-wind proceeded similarly to quasi-parallel shocks with a compression factor of 4 (this might be higher when CR escape effects are accounted for) and the characteristic shock velocity $\sim v_\mathrm{p}$.

The gas in the p-wind experiences oblique recollimation shocks and Mach disks driven by the isotropic wind, it is heated and experiences a sequence of compression and rarefactions. Similarly to the i-wind, the density of the shocked p-wind is far too low to produce appreciable thermal emission. We therefore relied on the possibility that recollimation shocks are effective in accelerating particles and that the EXJ emission is nonthermal (as suggested before, see, e.g., Safi-Harb et al. 2022, and references therein). The recent detection of X-ray polarization from EXJ (Kaaret et al. 2024) with IXPE indeed shows that X-ray emission has a synchrotron origin, while the magnetic field is largely along the eastern EXJ. The acceleration could be due to shocks (i.e., Diffusive Shock Acceleration or DSA Krymskii 1977; Bell 1978) or to a shear flow (Berezhko 1981; Stawarz & Ostrowski 2002; Rieger & Duffy 2019) that naturally appears in the configuration considered here. In both cases, it is plausible that the acceleration is not only confined to a localized region at the first recollimation shock, but is distributed along the EXJ.

The hard nonthermal X-ray emission up to 30 keV from a knotty region within the eastern EXJ was detected with the *NuSTAR* telescope and attributed to synchrotron radiation of very high energy electrons with Lorentz factors above 10^7 (Safi-Harb et al. 2022; Sudoh et al. 2020). These electrons have to be (re)accelerated locally. An ensemble of the recollimation shocks that have to be present after the collision of the p-wind with the termination shock of the i-wind is a plausible site of particle acceleration and magnetic field amplification. Nonthermal X-ray emission observed as thin filaments at the edge of the shell-type young supernova remnants is almost certainly produced by synchrotron emission of TeV regime electrons radiating in a highly amplified magnetic field (Reynolds 2008; Helder et al. 2012; Ferrazzoli et al. 2023). Particle acceleration by strong shocks with a velocity well above a few thousand km s^{-1} in young supernova remnants is likely accompanied by the strong amplification of magnetic fluctuations, resulting in Bohm-like diffusion of accelerated particles in a wide interval of particle energies (see, e.g., Bykov et al. 2014; Caprioli & Spitkovsky 2014). In the case of Bohm diffusion, the acceleration time t_a of a particle with a Lorentz factor γ by a shock of velocity v_p scales with the magnetic field strength B as $t_a \propto \gamma v_\mathrm{p}^{-2} \eta B^{-1}$. Here, the diffusion coefficient of a relativistic particle of mass m is $D = \eta c^2 m \gamma / eB$, where the dimensionless factor is $\eta \geq 1$. The maximum Lorentz factor that can be achieved by the electrons and positrons that are accelerated by the shock is limited by the synchrotron losses with $\gamma_\mathrm{m} \propto v_\mathrm{p} B^{-1/2} \eta^{-1/2}$. Therefore, in a single-zone model (where particle acceleration and the synchrotron radiation are

spatially coincident) the maximum energy of the synchrotron photon E_m mostly depends on the shock velocity $E_m \propto v_p^2/\eta$. To obtain $E_m \approx 30$ keV, we need $v_p \sim 20\,000\,\eta^{1/2}$ km s^{-1}. The energy flux of the amplified magnetic field in the shock downstream may reach 0.1 of the shock ram pressure (Bykov et al. 2014), which is consistent with observations of young supernova remnants (Helder et al. 2012). In this case, the magnetic field just downstream of the recollimation shock can be estimated from the relation $B^2/8\pi \approx 0.4\frac{L_p}{\Omega_i R_T^2 v_p}$. The magnitudes of the fluctuating magnetic field amplified by cosmic-ray-driven instabilities may reach ∼100 μG. Then the accelerated electrons radiating 30 keV synchrotron photons should have energies of ∼100 TeV. The spectra of electrons accelerated by the DSA Fermi mechanism are consistent with those derived from hard X-ray observations (Safi-Harb et al. 2022; Kayama et al. 2022).

When this paper was under revision, new results from H.E.S.S. observations of W50/SS433 became available (H.E.S.S. Collaboration 2024). From a model fitting of spatial profiles of the gamma-ray emission along the jet axis, the starting velocity for both the eastern and western jets was found to be $0.083(\pm 0.026\,\mathrm{stat} \pm 0.010\,\mathrm{syst})\,c \approx 25\,000$ km s^{-1}. Accelerated electrons are continuously injected with a power-law spectrum with an index 2 and a cutoff energy > 200 TeV at the outer jet base in the 1D propagation model discussed by H.E.S.S. Collaboration (2024). The leptons then travel along the jet and produce the observed radiation. The authors considered two models of the external jet propagation and estimated the diffusion coefficients of relativistic 100 TeV particles to be $(2.3 \pm 1.4) \times 10^{28}$ cm^2 s^{-1}, assuming a decelerating jet and $(4.7 \pm 4.1) \times 10^{27}$ cm^2 s^{-1} for a jet with a constant velocity. The model assumed a homogeneous magnetic field along the jets with a magnitude close to 20 μG. In the model we discussed above, the maximum RMS amplitude of a fluctuating magnetic field can be a few times higher and reach ∼100 μG in the shock recollimation region. The turbulent fluctuating field would decay outside the acceleration region where CR-driven instabilities amplify the field. The energies of the synchrotron X-ray emitting electrons can be ∼100 TeV.

Protons can be accelerated by the DSA mechanism with Bohm's diffusion in the shock vicinity to the maximum energies $E_{pm} \gtrsim$ PeV $v_{s01}\,R_{pc}\,B_{100}\,\eta^{-1}$, where v_{s01} is the shock velocity measured in units of 0.1 c, R_{pc} is the size of the acceleration region measured in pcs, and B_{100} is the magnitude of the turbulent magnetic field in the acceleration region, measured in units of 100 μG.

The protons accelerated above 100 TeV in the recollimation region will leave the accelerator and can contribute to multi-TeV regime emission detected by HAWC (Abeysekara et al. 2018) and LHAASO (Cao et al. 2024). Assuming a lifetime of EXJs of $\sim 10^4$–10^5 yr, these protons will radiate at about some tenths of a percent of their power due to inelastic hadronic collisions in ∼30 pc vicinity of the knot provided that the diffusion coefficient of the high-energy protons is $\sim 10^{27}$ cm^2 s^{-1}. The value is generally consistent with that estimated in the vicinity of typical TeV halos (see, e.g., Abeysekara et al. 2017; Martin et al. 2022; Fang 2024). We note here that the studied TeV halos are produced by the rotation power of pulsars (e.g., Geminga) with a much lower kinetic or magnetic luminosity than that of W50/SS433, which is powered by hyperaccretion. In this model, the power of the accelerated very high energy nuclei can reach $\sim 10^{37}$ erg s^{-1}. Eventually, these nuclei leave W50/SS433 and contribute to the galactic cosmic-ray population.

For the simplified quantitative estimates of particle acceleration and high-energy radiation given above, we limited ourselves to the DSA scenario. Nonlinear DSA models constructed for single-plane shocks account for cosmic-ray driven instabilities (see, e.g., Schure & Bell 2012) that may highly amplify the ambient magnetic field fluctuations and thus govern the high-energy particle transport. The recollimation of the p-wind is accompanied by the formation of a system of oblique shocks, and the description of particle acceleration in the wind recollimation region is more complex than the DSA model used above. Namely, the spectrum formation at the highest-energy end can be affected by CR interaction with the shear flows (see e.g. Rieger & Duffy 2019), which is associated with the p-wind recollimation region.

An accurate modeling of the particle spectra would require both high-resolution simulations of the recollimation region for different possible magnetization of the p-wind and a kinetic modeling of the high-energy particle transport in the region.

The simulations shown in Figs. 2 and A.1 are not intended as accurate models of the SS433/W50 system. They are used solely to illustrate a range of possible morphologies and to argue that in this hyperaccreting binary, an extended jet-like feature might arise naturally even in the absence of an SNR and the famous narrow 0.26 c jet, which are the focus in many other studies. We do not discuss the role of disk precession and a more realistic wind configuration either. We leave these issues and detailed high-resolution magnetohydrodynamic simulations of the setup discussed here for future studies.

4. Conclusions

We outlined a possible model of EXJs in the W50 nebula. At variance with other popular models, we did not associate these structures with the well-collimated 0.26 c baryonic jets produced by the hyperaccreting binary SS433. We instead proposed that a powerful anisotropic wind from the binary that was active for a few tens of kyr causes these structures (and the overall W50 morphology as well). In the simplest version of this model, the wind consists of two components: an almost isotropic wind that subtends most of the solid angle, and a more collimated polar wind. Both wind components are cold and invisible until the isotropic wind reaches its terminal shock. Beyond this point, a conical recollimation shock is launched into the polar wind component, which is capable of accelerating relativistic electrons that power the spectrally featureless and polarized synchrotron radiation that is visible in X-rays as EXJs.

The inner edges of the EXJs approximately correspond to the location of the first recollimation-shock knot. Plausibly, as suggested earlier, the TeV emission is produced by the same electrons due to IC scatterings of CMB photons. This model also associates the overall shape of the W50 nebula (a sphere plus two ears) with the same anisotropic wind, namely the forward shock of the wind propagating into the undisturbed ISM. The particular set of parameters used here for illustration is loosely constrained and likely does not exactly match those in W50. However, recollimation of the anisotropic wind offers an attractive explanation of the peculiar properties of the EXJs in SS433/W50. It is plausible that other hyperaccreting systems can give rise to similar structures as long as the wind has a sufficiently strong angular modulation pattern. The model also stipulates that W50 EXJs are powerful sources of very high-energy cosmic-ray protons, which are accelerated within the same converging flow region.

Acknowledgements. We thank our referee for many helpful and constructive comments. E.C. and I.K. are grateful to Selma E. de Mink and Stephen Justham for a useful discussion on the binary evolution of SS433-like systems. I.K. acknowledges support by the COMPLEX project from the European Research Council (ERC) under the European Union's Horizon 2020 research and innovation program grant agreement ERC-2019-AdG 882679. A.B. was supported by the baseline project FFUG-2024-0002 at Ioffe Institute. Some modeling was made at the Supercomputing Center of the Peter the Great Saint-Petersburg Polytechnic University.

References

Abeysekara, A. U., Albert, A., Alfaro, R., et al. 2017, Science, 358, 911
Abeysekara, A. U., Albert, A., Alfaro, R., et al. 2018, Nature, 562, 82
Aharonian, F. A., & Atoyan, A. M. 1998, New Astron. Rev., 42, 579
Alexander, P. 2006, MNRAS, 368, 1404
Asahina, Y., Ogawa, T., Kawashima, T., et al. 2014, ApJ, 789, 79
Barkov, M. V., & Bosch-Ramon, V. 2022, MNRAS, 510, 3479
Begelman, M. C., Sarazin, C. L., Hatchett, S. P., McKee, C. F., & Arons, J. 1980, ApJ, 238, 722
Begelman, M. C., King, A. R., & Pringle, J. E. 2006, MNRAS, 370, 399
Bell, A. R. 1978, MNRAS, 182, 147
Berezhko, E. G. 1981, Int. Cosmic Ray Conf., 3, 506
Blundell, K. M., & Bowler, M. G. 2004, ApJ, 616, L159
Blundell, K. M., Laing, R., Lee, S., & Richards, A. 2018, ApJ, 867, L25
Bowler, M. G., & Keppens, R. 2018, A&A, 617, A29
Brinkmann, W., Kotani, T., & Kawai, N. 2005, A&A, 431, 575
Brinkmann, W., Pratt, G. W., Rohr, S., Kawai, N., & Burwitz, V. 2007, A&A, 463, 611
Broderick, J. W., Fender, R. P., Miller-Jones, J. C. A., et al. 2018, MNRAS, 475, 5360
Bykov, A. M., Ellison, D. C., Osipov, S. M., & Vladimirov, A. E. 2014, ApJ, 789, 137
Calvani, M., & Nobili, L. 1981, Ap&SS, 79, 387
Cao, Z., Aharonian, F., An, Q., et al. 2024, ApJS, 271, 25
Caprioli, D., & Spitkovsky, A. 2014, ApJ, 794, 47
Cherepashchuk, A. M., Belinski, A. A., Dodin, A. V., & Postnov, K. A. 2021, MNRAS, 507, L19
Cherepashchuk, A., Belinski, A., Dodin, A., & Postnov, K. 2023, New Astron., 103, 102060
Chevalier, R. A., & Clegg, A. W. 1985, Nature, 317, 44
Churazov, E., Khabibullin, I., & Sunyaev, R. 2020, MNRAS, 495, L51
Drury, L. O., Ellison, D. E., Aharonian, F. A., et al. 2001, Space Sci. Rev., 99, 329
Dubner, G. M., Holdaway, M., Goss, W. M., & Mirabel, I. F. 1998, AJ, 116, 1842
Eichler, D. 1983, ApJ, 272, 48
Fabrika, S. 2004, Astrophys. Space Phys. Res., 12, 1
Fabrika, S., Ueda, Y., Vinokurov, A., Sholukhova, O., & Shidatsu, M. 2015, Nat. Phys., 11, 551
Fang, K. 2024, Phys. Rev. D, 109, 043041
Farnes, J. S., Gaensler, B. M., Purcell, C., et al. 2017, MNRAS, 467, 4777
Ferrazzoli, R., Slane, P., Prokhorov, D., et al. 2023, ApJ, 945, 52
Fogantini, F. A., García, F., Combi, J. A., et al. 2023, A&A, 669, A149
Goodall, P. T., Alouani-Bibi, F., & Blundell, K. M. 2011, MNRAS, 414, 2838
H.E.S.S. Collaboration (Olivera-Nieto, L., et al.) 2024, Science, 383, 402
Helder, E. A., Vink, J., Bykov, A. M., et al. 2012, Space Sci. Rev., 173, 369
Hjellming, R. M., & Johnston, K. J. 1981, ApJ, 246, L141
Kaaret, P., Ferrazzoli, R., Silvestri, S., et al. 2024, ApJ, 961, L12
Kayama, K., Tanaka, T., Uchida, H., et al. 2022, PASJ, 74, 1143
Khabibullin, I. I., & Sazonov, S. Y. 2017, Astron. Lett., 43, 388
Khabibullin, I., Medvedev, P., & Sazonov, S. 2016, MNRAS, 455, 1414
Kimura, S. S., Murase, K., & Mészáros, P. 2020, ApJ, 904, 188
Komissarov, S. S., & Falle, S. A. E. G. 1998, MNRAS, 297, 1087
Konigl, A. 1983, MNRAS, 205, 471
Krause, M., Alexander, P., Riley, J., & Hopton, D. 2012, MNRAS, 427, 3196
Krymskii, G. F. 1977, Akademiia Nauk SSSR Doklady, 234, 1306
López-Miralles, J., Perucho, M., Martí, J. M., Migliari, S., & Bosch-Ramon, V. 2022, A&A, 661, A117
Margon, B. 1984, ARA&A, 22, 507
Marshall, H. L., Canizares, C. R., & Schulz, N. S. 2002, ApJ, 564, 941
Marshall, H. L., Canizares, C. R., Hillwig, T., et al. 2013, ApJ, 775, 75
Martin, P., Tibaldo, L., Marcowith, A., & Abdollahi, S. 2022, A&A, 666, A7
Medvedev, A., & Fabrika, S. 2010, MNRAS, 402, 479
Medvedev, P. S., Khabibullin, I. I., & Sazonov, S. Y. 2019, Astrono. Lett., 45, 299
Meyer, D. M. A. 2024, MNRAS, 530, 539
Migliari, S., Fender, R., & Méndez, M. 2002, Science, 297, 1673
Migliari, S., Fender, R. P., Blundell, K. M., Méndez, M., & van der Klis, M. 2005, MNRAS, 358, 860
Mignone, A., Bodo, G., Massaglia, S., et al. 2007, ApJS, 170, 228
Miller-Jones, J. C. A., Migliari, S., Fender, R. P., et al. 2008, ApJ, 682, 1141
Monceau-Baroux, R., Porth, O., Meliani, Z., & Keppens, R. 2015, A&A, 574, A143
Ohmura, T., Ono, K., Sakemi, H., et al. 2021, ApJ, 910, 149
Panferov, A. A. 2017, A&A, 599, A77
Parizot, E., Marcowith, A., van der Swaluw, E., Bykov, A. M., & Tatischeff, V. 2004, A&A, 424, 747
Perucho, M., & López-Miralles, J. 2023, J. Plasma Phys., 89, 915890501
Peter, W., & Eichler, D. 1993, ApJ, 417, 170
Poutanen, J., Lipunova, G., Fabrika, S., Butkevich, A. G., & Abolmasov, P. 2007, MNRAS, 377, 1187
Rankin, J. S., Bindi, V., Bykov, A. M., et al. 2022, Space Sci. Rev., 218, 42
Reynolds, S. P. 2008, ARA&A, 46, 89
Reynoso, M. M., Romero, G. E., & Christiansen, H. R. 2008, MNRAS, 387, 1745
Rieger, F. M., & Duffy, P. 2019, ApJ, 886, L26
Safi-Harb, S., & Ögelman, H. 1997, ApJ, 483, 868
Safi-Harb, S., & Petre, R. 1999, ApJ, 512, 784
Safi-Harb, S., Mac Intyre, B., Zhang, S., et al. 2022, ApJ, 935, 163
Schure, K. M., Bell, A. R., & O'C Drury, L., & Bykov, A. M., 2012, Space Sci. Rev., 173, 491
Shakura, N. I., & Sunyaev, R. A. 1973, A&A, 24, 337
Stawarz, Ł., & Ostrowski, M. 2002, ApJ, 578, 763
Sudoh, T., Inoue, Y., & Khangulyan, D. 2020, ApJ, 889, 146
van den Heuvel, E. P. J., Portegies Zwart, S. F., & de Mink, S. E. 2017, MNRAS, 471, 4256
Velázquez, P. F., & Raga, A. C. 2000, A&A, 362, 780
Waisberg, I., Dexter, J., Olivier-Petrucci, P., Dubus, G., & Perraut, K. 2019, A&A, 624, A127
Watson, M. G., Willingale, R., Grindlay, J. E., & Seward, F. D. 1983, ApJ, 273, 688
Yamauchi, S., Kawai, N., & Aoki, T. 1994, PASJ, 46, L109
Yoshioka, S., Mineshige, S., Ohsuga, K., Kawashima, T., & Kitaki, T. 2022, PASJ, 74, 1378
Zavala, J., Velázquez, P. F., Cerqueira, A. H., & Dubner, G. M. 2008, MNRAS, 387, 839
Zealey, W. J., Dopita, M. A., & Malin, D. F. 1980, MNRAS, 192, 731

Appendix A: W50 morphology for different wind parameters

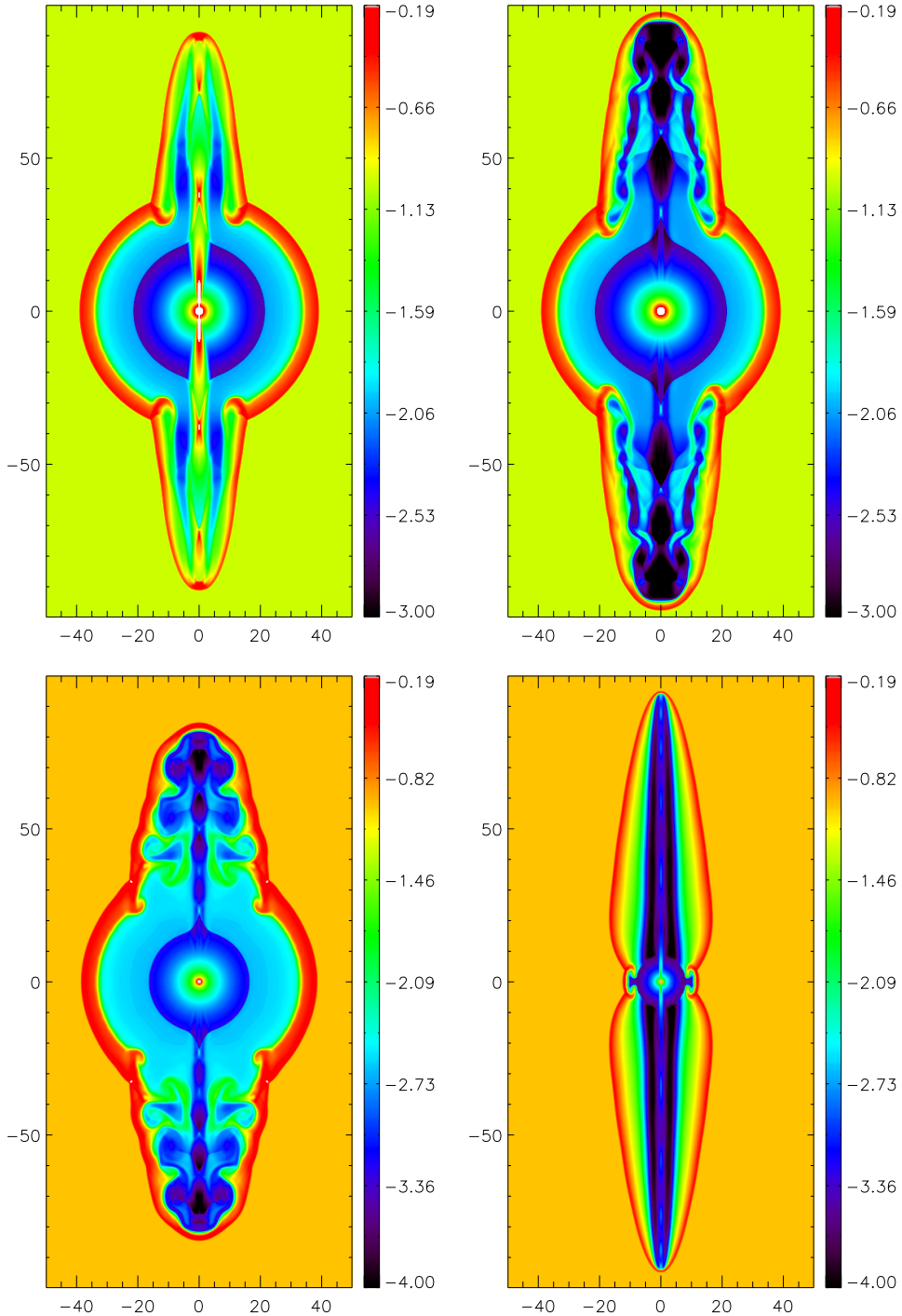

Fig. A.1. Density slices for different wind configurations. The color corresponds to $\log_{10}(\rho)$, where ρ is in units of m_p/cm^3, and the color-coding is different for the top and bottom rows. The top two panels use the same parameters of the i-wind, $L_i = 10^{39}\,\mathrm{erg\,s^{-1}}$, $v = 2\times10^3\,\mathrm{km\,s^{-1}}$, but different initial p-wind densities and velocities. In the left panel, the p-wind velocity is the same as in the i-wind, but the density is 60 times higher, and in the right panel, the density is the same as in the i-wind, but the velocity is higher by a factor of 6, i.e., $\sim 1.2\times10^4\,\mathrm{km\,s^{-1}}$. The bottom left panel shows a simulation for twice higher i- and p-wind velocities, $4\times10^3\,\mathrm{km\,s^{-1}}$ and $\sim 2.4\times10^4\,\mathrm{km\,s^{-1}}$, respectively. Finally, the bottom right panel shows the case when the i-wind is much weaker than in the bottom left panel. In this case, the jet behavior follows a self-similar solution, when the underdense jet is recollimated by its cocoon. In all simulations, the half-opening angle of the p-wind was the same, $\sim 4-5^\circ$

To better illustrate the difference between the proposed anisotropic wind model for W50 from a bare jet in a uniform medium, we ran four simulations with varying i- and p-wind parameters (Fig. A.1). In all runs, the parameters of the ambient medium were the same, and the effective half-opening angle θ of the p-wind was set to $\sim 4°$. This value of θ also characterizes a smooth transition between the two wind components. This was done by modulating the angular dependence of the p- and i-winds by $f(\theta)$ and $(1 - f(\theta))$, respectively, where $f(\theta) = \cos^n \theta$. Here, the value of n controls the confinement angle (see Fig. 2 for an example of a purely conical i-wind). For the simulations shown in Fig. A.1, $n = 256$ was used and $f(\theta) = 0.5$ for $\theta = 4.2°$.

The i- and p-winds were initiated within a sphere with a radius $r = 8$ pc. The top row compares the cases when the p-wind has the same velocity as the i-wind, but a density 60 times higher (top left panel) and the case when the i-wind has the same density, but a velocity a factor of 6 higher (top right panel). Broadly, the first case illustrates dense streams of the Haro-Herbig-type, while the second case is more reminiscent of fast extragalactic jets. The kinetic luminosities of the p-wind $L_p \propto \Omega_p \rho_p v_p^3$ vary from one panel to the next. In the top left panel, $L_p \sim 0.23\, L_i$, in the top right and bottom left panels, $L_p \sim 0.84\, L_i$. For these three panels, $L_i = 10^{39}\,\mathrm{erg\,s^{-1}}$. In the bottom right panel, the kinetic power of the isotropic wind is very low, while L_p is $0.84 \times 10^{39}\,\mathrm{erg\,s^{-1}}$.

The top left panel illustrates the dense-jet case when the p-wind remains strongly overdense with respect to the i-wind even when the latter passes through its termination shock and becomes four times denser. In this case, no cocoon is expected to form, and the recollimation is purely driven by the increased pressure of the i-wind. In this run, the ears have a relatively simple morphology due to the high momentum of the p-wind.

For the lighter p-wind (top right panel), the p-wind recollimates itself early on, followed by further recollimation after the i-wind termination shock. After crossing the forward shock, this lighter p-wind creates a sequence of eddies in the ears.

The bottom left panel uses a similar setup of a light p-wind, but the velocities of the i- and p-winds are increased by a factor of 2 while keeping the same kinetic luminosities. As expected, the radius of the i-wind terminal shock reduces by a factor $\sim \sqrt{2}$ and so does the recollimation region of the p-wind. Except for these changes, the overall morphology remains qualitatively similar to that in the top right panel.

Finally, the bottom right panel shows the case when the i-wind is far weaker than the p-wind, whose parameters are the same as in the bottom left panel. In this case, the p-wind follows the canonical self-similar pattern expected for underdense jets (e.g., Komissarov & Falle 1998; Alexander 2006; Krause et al. 2012). It develops its own cocoon that recollimates the jet, which then propagates through the uniform medium. The jet keeps a very regular morphology and propagates faster than in the other cases. The time of the snapshot is ~ 48 kyr, that is, earlier than for other panels (~ 60 kyr).

This comparison shows that anisotropic winds can broadly reproduce the morphology of W50 and can feature a recollimation shock inside the forward shock of the i-wind. The complicated substructure of the soft X-ray emission in the lobes of W50 seems to favor lighter and faster p-wind scenarios (see Fig. A.1), which are broadly consistent with simulations of super-Eddington flows (e.g., Yoshioka et al. 2022). However, the parameters of the actual outflow from SS433 might be much more complicated, especially when the disk precession is considered, and some of the parameters, such as the opening angle of the p-wind, were set by hand. While these axisymmetric pure hydrodynamical simulations clearly represent a gross oversimplification of the real system, they illustrate the main idea of this study.

Appendix B: Role of the SNR

As discussed in the main text, our baseline model assumed that the quasi-spherical part of the W50 nebula is created by the isotropic part of the hyperaccreting compact object on a timescale of ~ 60 kyr rather than by the supernova explosion that produced the black hole. In our model, the supernova explosion occurred a long time ago (millions of years). However, some scenarios assume that this supernova is a more recent event $\sim 10^5$ yr (e.g., Goodall et al. 2011; Panferov 2017; Bowler & Keppens 2018). We briefly consider the case when an isotropic wind propagates through the still-expanding supernova remnant (SNR). Basically, we consider a type II supernova (ejecta mass $20\, M_\odot$, ejecta kinetic energy 10^{51} erg) in a uniform medium and then initiate an isotropic wind with some delays (2000 and 10000 yr) after the SN explosion. The corresponding pressure profiles are shown in Fig. B.1. All cases are shown at a time when the forward shock reaches $r \sim 38$ pc, which is the observed size of the W50 quasi-spherical part. For comparison, two pure-wind profiles for different wind velocities are also shown. In all cases, the kinetic power of the isotropic wind is the same ($10^{39}\,\mathrm{erg\,s^{-1}}$). This figure clearly shows that in the presence of the SNR, the forward-shock region does not change much, although it takes less time than the case of the wind alone. The position of the wind termination is not affected, which is the main point of the model considered here.

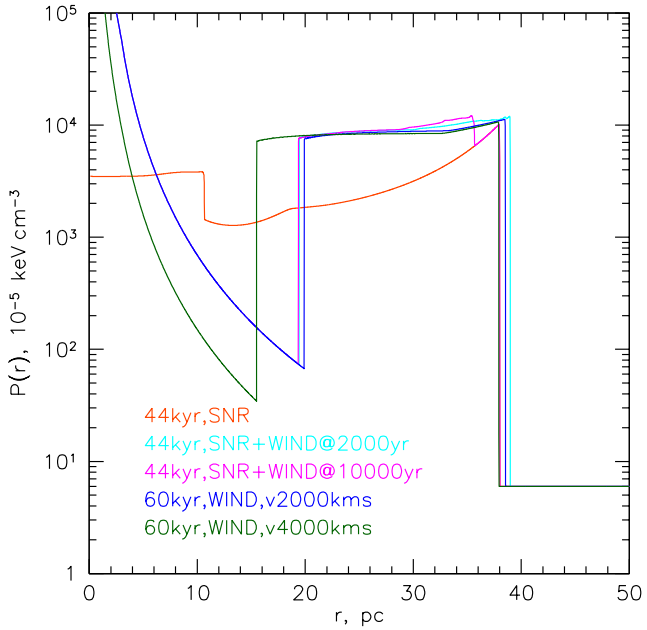

Fig. B.1. Comparison of the gas-pressure profiles for cases with and without a prior supernova explosion. The blue line shows the case of the isotropic wind operating for 60 kyr in a uniform medium (same as shown in Fig.1). The red line shows the pressure profile that would appear if a type II supernova (ejecta mass 20 $M_\odot$, ejecta kinetic energy 10^{51} erg) exploded in the same environment. In this case, the forward shock would reach the same radius in $\sim$ 44 kyr. The edges in the red curve at radii between 10 and 20 pc are the artifacts of the 1D model caused by the reflection of the reserve shock from the center. Finally, the cyan and magenta lines show the pressure profiles when the wind starts to operate 2000 and 10,000 yr after the SNR explosion, respectively. In these cases, the profiles shown correspond to 44 kyr since the onset of the supernova. In all cases, a large pressure jump is present at the position of the wind termination shock. The only noticeable effect of the SNR is that the forward shock reaches $r \sim 40$ pc in a shorter time (44 kyr vs. 60 kyr). Finally, the green line shows the case of a twice faster wind (4000 vs 2000 km s^{-1}). As expected, the position of the termination shocks moves closer to the source. Comparison of the gas-pressure profiles for cases with and without a prior supernova explosion. The blue line shows the case of the isotropic wind operating for 60 kyr in a uniform medium (same as shown in Fig.1). The red line shows the pressure profile that would appear if a type II supernova (ejecta mass 20 $M_\odot$, ejecta kinetic energy 10^{51} erg) exploded in the same environment. In this case, the forward shock would reach the same radius in $\sim$ 44 kyr. The edges in the red curve at radii between 10 and 20 pc are the artifacts of the 1D model caused by the reflection of the reserve shock from the center. Finally, the cyan and magenta lines show the pressure profiles when the wind starts to operate 2000 and 10,000 yr after the SNR explosion, respectively. In these cases, the profiles shown correspond to 44 kyr since the onset of the supernova. In all cases, a large pressure jump is present at the position of the wind termination shock. The only noticeable effect of the SNR is that the forward shock reaches $r \sim 40$ pc in a shorter time (44 kyr vs. 60 kyr). Finally, the green line shows the case of a twice faster wind (4000 vs 2000 km s^{-1}). As expected, the position of the termination shocks moves closer to the source.